Flow-Thermal-Structural Study of Aerodynamically Heated Leading Edges

Pramote Dechaumphai*
NASA Langley Research Center, Hampton, Virginia
Earl A. Thornton†
Old Dominion University, Norfolk, Virginia
and
Allan R. Wieting‡
NASA Langley Research Center, Hampton, Virginia

An integrated fluid-thermal-structural finite-element approach is applied to the analysis of aerodynamically heated leading edges. The Navier-Stokes equations for high-speed compressible flow, the energy equation, and the quasistatic equilibrium equations for the leading edge are solved using a single finite-element approach in one integrated, vectorized computer program. The fluid-thermal-structural coupling is studied for Mach 6.47 flow over a 3-in.-diam cylinder for which the flow behavior and the aerothermal loads are calibrated by experimental data. Issues of the thermal structural response are studied for hydrogen-cooled, superthermal conducting leading edges subjected to intense aerodynamic heating.

Nomenclature

A = coolant passage area, Eq. (5), or finite-element area, Eq. (10)
c = specific heat, Eqs. (4) and (5), or fictitious damping constant, Eq. (7)
E,F = x and y flux components
H = heat load
h = convective heat-transfer coefficient
k = thermal conductivity
l,m = components of unit normal vector
$\dot{m}$ = coolant mass flow rate
$[M]$ = mass matrix
$[N]$ = element interpolation function
P = coolant passage perimeter
p = pressure
q = heat flux
$\{R\}$ = load vector
T = temperature
T_0 = reference temperature for zero stress
T_r = fluid recovery temperature
T_∞ = surrounding medium temperature
t = time
Δt = time step
U = conservation variable
u,v = flow velocity components, Eq. (2), or displacement components, Eq. (7)
x,y = coordinate directions
ρ = density
ϵ = flow total energy, Eq. (2), or strain components, Eq. (19), or emissivity, Eq. (20)
σ = Stefan-Boltzmann constant
$\sigma_x, \sigma_y, \tau_{xy}$ = fluid stress components, Eq. (2), or solid stress components, Eq. (7)

Subscripts
F = fluid
T = thermal
s = structural

Superscripts
I = inviscid
T = transpose
V = viscous
n = time-step index

Presented as Paper 88-2245 at the AIAA/ASME/ASCE/AHS/ASC 29th Structures, Structural Dynamics and Materials Conference, Williamsburg, VA, April 18-20, 1988; received June 19, 1988; revision received March 20, 1989.

*Aerospace Technologist, Aerothermal Loads Branch, Structural Mechanics Division. Member AIAA.
†Professor, Department of Mechanical Engineering and Mechanics. Associate Fellow AIAA.
‡Head, Aerothermal Loads Branch, Structural Mechanics Division. Member AIAA.

Introduction

DESIGN of lightweight structures and thermal protection systems for hypersonic cruise and re-entry vehicles depends on accurate prediction of the aerothermal loads, structural temperatures and their gradients, and the structural deformations and stresses. Traditionally, an aerodynamicist will predict the surface pressures and heating rates assuming a rigid isothermal body. These aerodynamic heating rates are used by a structural heat-transfer analyst to predict the structural temperature distribution. Finally, a structural analyst uses the temperature distribution and aerodynamic pressures to predict the structural deformations and stresses. Such traditional independent approaches require several iterations between the different analysis methods and analysts. The approach is relatively inefficient because the incompatible mathematical models require extensive postprocessing to transfer data. Moreover, the interdisciplinary coupling and interactions, which are not insignificant, are rarely attempted because the iterative process not only requires several additional solutions but also remodeling in each analysis. The coupling occurs primarily through the thermal response of the structure because 1) the surface temperature affects the external flow by changing the amount of energy absorbed by the structure, and 2) the temperature gradients in the structure result in structural deformations that alter the aerodynamic surface and, hence, the flowfield and attendant surface pressures and heating rates. Hence, an integrated interdisciplinary

analysis procedure that would provide accurate, timely prediction of the coupled response is highly desirable.

The interdisciplinary coupling and interaction has been demonstrated in the design of high-speed vehicle structures. One such structure, a metallic thermal protection system (TPS) panel[1] for re-entry vehicles, thermally bows into the airstream to relieve thermal stresses. The bowing creates an aerodynamic surface consisting of arrays of spherical dome protuberances. As a first step to understanding the effect of the structural deformation on a hypersonic flowfield caused by the interactions, the aerothermal loads on a dome surface in a Mach 6.5 stream were predicted computationally[2] and measured experimentally.[3] These studies showed that the dome configuration caused complex shock and expansion waves and attendant localized heating rates that were 2–6 times higher than those for a uniform flat surface. The existence of the high localized heating rates indicates that several more iterations between interdisciplinary analyses would be required to converge the aerothermostructural response of the TPS. Typically, these additional calculations were never performed.

To further understand the coupled fluid-thermal-structural interactions, a thin panel representing a typical sidewall of an actively cooled engine structure has been analyzed with an integrated fluid-thermal-structural procedure.[4] The coupled analysis showed that the aerodynamic flowfield was altered 1) as the initial uniform wall temperature became nonlinear, and 2) as the panel deformed. The nonlinear temperature distribution and panel deformation not only changed the stress distribution in the panel, but also induced a complex external flow phenomenon consisting of separated flow with shocks and flow expansions.

Leading edges for hypersonic vehicles that experience intense stagnation point pressures and heating rates are often a challenge to the designer. For engine leading edges such as cowls or the fuel injection strut shown in Fig. 1, the intense loads can be amplified by an order of magnitude[5] when the leading-edge bow shock is impinged upon by an oblique shock wave. The intense localized heating causes severe temperature levels and gradients. This makes the analytical prediction difficult because of the strong nonlinearity that is present in all phases of the thermal and structural analyses.

The purposes of this paper are to 1) study the coupled fluid-thermal-structural behavior for aerodynamically heated leading edges using the technique developed for the heated panels, and 2) identify critical issues for integrated fluid-thermal-structural analysis. The solution of the Navier-Stokes equations for predicting aerodynamic heating and the solution for the associated thermal-structural equations are obtained using a Taylor-Galerkin algorithm in one integrated, vectorized computer program. The fluid-thermal-structural formulation and the solution approach are described. The integrated analysis will be demonstrated on a 3-in.-diam cylinder used to obtain the experimental pressures and heat-transfer rates to which the predictions will be compared. The issues associated with nonlinear thermal-structural response due to intense aerodynamic heating will be demonstrated by studies of a hydrogen-cooled leading edge subjected to shock wave interference heating. The latter example will identify the issues associated with the effects of severe temperature gradients on material property variations and thermal stresses.

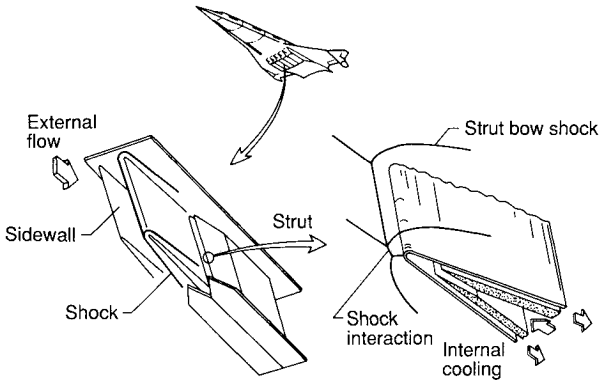

Fig. 1 Fluid-thermal-structural interactions on an aerospace plane scramjet engine leading edge.

Fluid-Thermal-Structural Equations

Aerodynamic Flow

The equations for a laminar compressible flow are described by the conservation of mass, momentum, and energy equations. These equations can be written in the conservation form as

$$\frac{\partial}{\partial t}\{U_F\} + \frac{\partial}{\partial x}\{E_F\} + \frac{\partial}{\partial y}\{F_F\} = 0 \tag{1}$$

where the subscript F denotes the flow analysis, $\{U_F\}$ is the vector of the conservation variables; $\{E_F\}$ and $\{F_F\}$ are vectors of the flux components in the x and y directions. These vectors are given by

$$\{U_F\}^T = [\rho \quad \rho u \quad \rho v \quad \rho \epsilon] \tag{2a}$$

$$\{E_F\}^T = [E_F]^I + [E_F]^V$$

$$= [\rho u \quad \rho u^2 + p \quad \rho uv \quad \rho u\epsilon + pu]$$

$$- [0 \quad \sigma_x \quad \tau_{xy} \quad u\sigma_x + v\tau_{xy} - q_x] \tag{2b}$$

$$\{F_F\}^T = [F_F]^I + [F_F]^V$$

$$= [\rho v \quad \rho uv \quad \rho v^2 + p \quad \rho v\epsilon + pv]$$

$$- [0 \quad \tau_{xy} \quad \sigma_y \quad u\tau_{xy} + v\sigma_y - q_y] \tag{2c}$$

Superscripts I and V represent the inviscid and viscous flux vector components, respectively. In the inviscid flux components, the pressure p is related to the total energy assuming a calorically perfect gas (constant ratio of specific heats). In the viscous flux components, the stresses σ_x, σ_y, and τ_{xy} are related to the velocity gradients assuming Stokes' hypothesis.[6] The heat fluxes q_x and q_y are related to the temperature gradients by Fourier's law, The temperature-dependent viscosity is computed from Sutherland's law,[6] and the thermal conductivity is computed assuming a constant Prandtl number of 0.72.

Structural Heat Transfer

The thermal response of the structure is described by the energy equation that can be written in conservation form as

$$\frac{\partial}{\partial t}(U_T) + \frac{\partial}{\partial x}(E_T) + \frac{\partial}{\partial y}(F_T) = H_T \tag{3}$$

where the subscript T denotes the thermal analysis, U_T is the conservation variable, E_T and F_T are the flux components, and H_T is the heat load. For transient heat conduction without internal heat source, these quantities are

$$U_T = \rho_s c_s T_s, \qquad E_T = q_x$$

$$F_T = q_y, \qquad H_T = 0 \tag{4}$$

where the subscript s denotes material quantities. The heat fluxes q_x and q_y are related to temperature gradients by Fourier's law.

For a convectively cooled structure, the thermal mass transport by the coolant is prescribed by an energy conservation equation based on 1) a bulk coolant temperature, 2) a convective heat-transfer coefficient that represents the thermal conductance between the structure and the coolant, and 3) the

coolant mass flow rate.[7] The energy equation for the coolant flow in the local x direction can be written in the form of Eq. (3) where

$$U_T = \rho_F c_F T_F, \qquad E_T = \dot{m} c_F T_F / A_F - k_F \partial T_F / \partial x$$

$$F_T = 0, \qquad H_T = hP(T_S - T_F) \tag{5}$$

The heat flux E_T consists of the energy transport by convection (1st term) and conduction (2nd term), and H_T represents the heat transfer between the structure and the coolant.

Structural Response

The structural response is described by the quasistatic equilibrium equations that can be written in conservation form as

$$\frac{\partial}{\partial t}\{U_s\} + \frac{\partial}{\partial x}\{E_s\} + \frac{\partial}{\partial y}\{F_s\} = 0 \tag{6}$$

where the subscript s denotes the structural analysis, $\{U_S\}$ is the displacement vector; $\{E_S\}$ and $\{F_S\}$ are vectors of the stress components and are given by

$$\{U_S\}^T = [cu \qquad cv]$$

$$\{E_S\}^T = [-\sigma_x \qquad -\tau_{xy}]$$

$$\{F_S\}^T = [-\tau_{xy} \qquad -\sigma_y] \tag{7}$$

where u and v are displacement components in the x and y directions, respectively; c is a fictitious damping constant used to facilitate marching to a steady-state quasistatic solution. The panel stress components σ_x, σ_y, and τ_{xy} are related to the displacement gradients and the temperature by the generalized Hooke's law.

Solution Procedure

An explicit time-marching finite-element scheme, the Taylor-Galerkin algorithm described in Ref. 4, is used to solve the fluid-thermal-structural equations (1-7). The algorithm offers several benefits in the analysis computation and permits convenient coupling between the analysis disciplines. The basic concept of the Taylor-Galerkin algorithm is to use 1) Taylor-series expansion in time to establish recurrence relations for time marching, and 2) the method of weighted residuals with Galerkin's criterion for spatial discretization. The fluid, thermal, and structural conservation equations are written in the form of a scalar equation

$$\frac{\partial U}{\partial t} + \frac{\partial E}{\partial x} + \frac{\partial F}{\partial y} = 0 \tag{8}$$

The key feature of the algorithm is to express the variation of the element fluxes E and F in the same form as the element dependent variable U,[8] i.e.,

$$U(x,y,t) = [N(x,y)]\{U(t)\}$$

$$E(x,y,t) = [N(x,y)]\{E(t)\}$$

$$F(x,y,t) = [N(x,y)]\{F(t)\} \tag{9}$$

where $[N(x,y)]$ denotes the element interpolation functions, and $\{U\}$, $\{E\}$, and $\{F\}$ are the vectors of the element nodal quantities.

Fluid Analysis

The two-time-level Taylor-Galerkin algorithm is used in the fluid analysis to provide numerical stability for the flow solution. The computation proceeds through two time levels $t_{n+1/2}$ and t_{n+1}. At time level $t_{n+1/2}$, values of $U^{n+1/2}$ are assumed constant within each element and are computed from

$$AU^{n+1/2} = \int_A [N]\, dA\, \{U\}^n - \frac{\Delta t}{2}\left(\int_A \left[\frac{\partial N}{\partial x}\right] dA\, \{E\}^n + \int_A \left[\frac{\partial N}{\partial y}\right] dA\, \{F\}^n\right) \tag{10}$$

At time level t_{n+1}, the nodal values of U^{n+1} are computed assuming a linear-element variation. The final equations are in the form

$$[M]\{\Delta U_F\}^{n+1} = \{R_F\}_1^n + \{R_F\}_2^n + \{R_F\}_3^{n+1/2} \tag{11}$$

where $\Delta U^{n+1} = U^{n+1} - U^n$, and $[M]$ denotes the mass matrix

$$[M] = \int_A \{N\}[N]\, dA \tag{12}$$

The first two vectors on the right-hand side of Eq. (11) represent the viscous flux within the element area and across the element boundary

$$\{R_F\}_1^n = -\Delta t\left(\int_A \left\{\frac{\partial N}{\partial x}\right\}[N]\, dA\, \{E^V\}^n + \int_A \left\{\frac{\partial N}{\partial y}\right\}[N]\, dA\, \{F^V\}^n\right) \tag{13}$$

$$\{R_F\}_2^n = \Delta t \int_s \{N\}[N]\, ds(l\{E^V\}^n + m\{F^V\}^n) \tag{14}$$

The last vector on the right-hand side of Eq. (11) represents both the inviscid and viscous fluxes computed from the element quantities $U^{n+1/2}$ at time level $t_{n+1/2}$. All matrices in Eqs. (10-14) are evaluated in closed form.[9] To produce an explicit algorithm, the mass matrix $[M]$ in Eq. (12) is diagonalized.

Thermal Analysis

For the thermal analysis, a single-time-level version of the algorithm is used.[10] Derivation of the element equations proceeds in the same fashion as described for the flow analysis. The final-element equations are in the form

$$[M]\{\Delta U_T\}^{n+1} = \{R_T\}_1^n + \{R_T\}_2^n \tag{15}$$

where

$$\{R_T\}_1^n = \Delta t\left(\int_A \left\{\frac{\partial N}{\partial x}\right\}[N]\, dA\, \{E_T\}^n + \int_A \left\{\frac{\partial N}{\partial y}\right\}[N]\, dA\, \{F_T\}^n\right) \tag{16}$$

$$\{R_T\}_2^n = -\Delta t \int_s \{N\}[N]\, ds(l\{E_T\}^n + m\{F_T\}^n) = -\Delta t \int_s \{N\}[N]\, ds\{q\}^n \tag{17}$$

The vectors $\{E_T\}$ and $\{F_T\}$ contain the element nodal heat-flux components. The vector $\{q\}$ in Eq. (17) represents nodal heat fluxes normal to the element surface boundary. Typical nodal heat-flux components, for an isotropic material as an example, are computed from Fourier's law:

$$E_T = q_x = -k(T)\frac{\partial T}{\partial x} \tag{18a}$$

$$F_T = q_y = -k(T)\frac{\partial T}{\partial y} \tag{18b}$$

The nodal temperature gradients $\partial T/\partial x$ and $\partial T/\partial y$ depend on element types and element nodal temperatures and can be computed explicitly. Benefits of the Taylor-Galerkin algorithm include 1) all element matrices and element nodal quantities can be evaluated in closed form, i.e., numerical integration is not required, even for quadrilateral elements, 2) material nonlinearity such as temperature-dependent thermal conductivity can be included directly [Eq. (18)], 3) nonlinear boundary conditions that will be described in the subsequent section can be implemented easily, and 4) an explicit time-marching scheme can be used for transient nonlinear analysis, if preferred, thus avoiding the iterative solution of a set of simultaneous equations.

Structural Analysis

The same approach used for the thermal analysis is applied to derive the finite-element equations for the structural analysis.[10] The equations are identical to Eqs. (15–17) except that the subscript T is replaced by the subscript s everywhere. The vectors $\{E_s\}$ and $\{F_s\}$ now represent the element nodal stress components. For an elastic orthotropic material, typical nodal stress components in two dimensions are obtained using constitutive relations

$$\sigma_i = c_{ij}\epsilon_j + \beta_i(T - T_0), \qquad i,j = 1,2,3 \tag{19}$$

where T_0 is the reference temperature for zero thermal stress. The material elastic constants c_{ij} and the thermal expansion parameters β_i may be temperature dependent. Large-strain displacement relations can be included in the computation of the strain components ϵ_j.

The explicit Taylor-Galerkin procedure described herein is conditionally stable. The allowable time steps depend on the size of elements and the characteristics of the problem. Guidelines for determining allowable time steps have been established and can be found in Refs. 10 and 11.

Initial and Boundary Conditions

The fluid, thermal, and structural Eqs. (1), (3), and (6) are solved subject to appropriate initial and boundary conditions. The initial conditions for these problems consist of specifying the distributions of the conservation variables $\{U\}$ at time zero. The boundary conditions for supersonic flow consist of specifying all conservation variables along the inflow surfaces. On supersonic outflow surfaces, the finite-element formulation provides appropriate boundary conditions. A no-slip condition (velocities set to zero) is specified at the solid surface.

The boundary conditions for the thermal analysis are applied via the vector shown in Eq. (15) and expressed in Eq. (17). The surface nodal heat flux q is replaced by the quantities representing different types of thermal boundary conditions:

$$q = \begin{cases} 0 & \text{(insulated)} \\ q_s & \text{(specified heating)} \\ h(T_s - T_r) & \text{(surface convection)} \\ \epsilon\sigma(T_s^4 - T_\infty^4) & \text{(surface radiation)} \end{cases} \tag{20}$$

The boundary conditions for the structural analysis, such as the applied pressure, can be added into the structural equations via the surface boundary vector. The procedure is identical to that for the thermal analysis previously described and is therefore omitted.

Coupled Fluid-Thermal Analysis

The Taylor-Galerkin approach permits the different analysis disciplines to be combined easily for the coupled analysis. As an example, the coupled solution for the flow/structure interface temperature can be solved from the equation that combines the flow energy [Eq. (11)] and the structural energy [Eq. (15)]. By applying the continuity condition of the heat flux across the interface, the final equations are in the form

$$[M_F]\{\rho_F c_F \Delta T\}^{n+1} + [M_S]\{\rho_S c_S \Delta T\}^{n+1} = \{R_F\}_1^n + \{R_T\}_1^n \tag{21}$$

These equations are solved for the temperature increment ΔT along the flow/structure interface. The final temperature $T^{n+1} = T^n + \Delta T^{n+1}$ represents the temperature valid for both the flowfield and the structure and provides continuity of heat flux across the flow/structure interface.

Applications

Two applications are presented to study the fluid-thermal-structural behavior of aerodynamically heated leading edges. A 3-in.-diam stainless steel cylinder subjected to aerodynamic heating from a Mach 6.47 flow is used as the first example to demonstrate the integrated analysis and validate predicted surface pressure and heating rates with experiment. The second example is a study of the thermal-structural response of a 0.25-in.-diam hydrogen-cooled leading edge subjected to intense shock wave interference heating. Critical issues for integrated fluid-thermal-structural analysis and design of the leading edges are identified.

Mach 6.47 Flow over a Cylinder

The solution to Mach 6.47 flow over a cylinder is used to demonstrate the integrated flow-thermal-structural analysis approach and validate the analytical prediction of the aerothermal loads. A schematic of the experiment, performed in the NASA Langley 8-ft High Temperature Tunnel, is shown in Fig. 2. A 3-in.-diam, 0.5-in.-thick, stainless steel cylinder was mounted on the panel holder and subjected to a uniform high-enthalpy Mach 6.47 flow. Details of the experimental

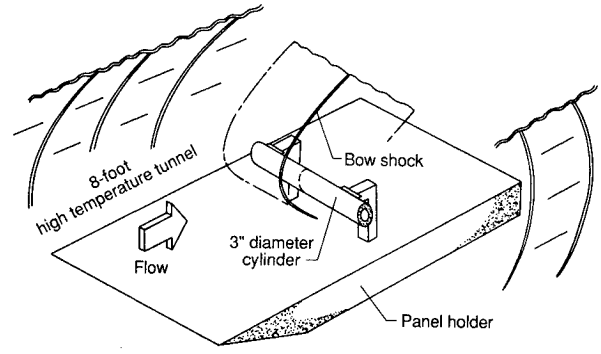

Fig. 2 Experimental configuration for flow over a 3-in.-diam cylinder in the 8-ft high temperature tunnel.

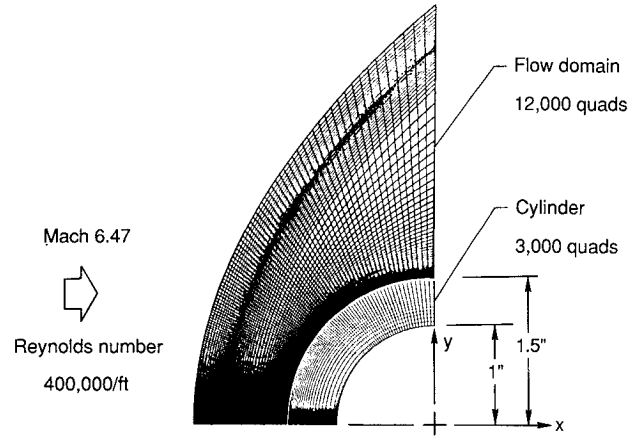

Fig. 3 Fluid-thermal-structural finite-element model for flow over a 3-in.-diam cylinder.

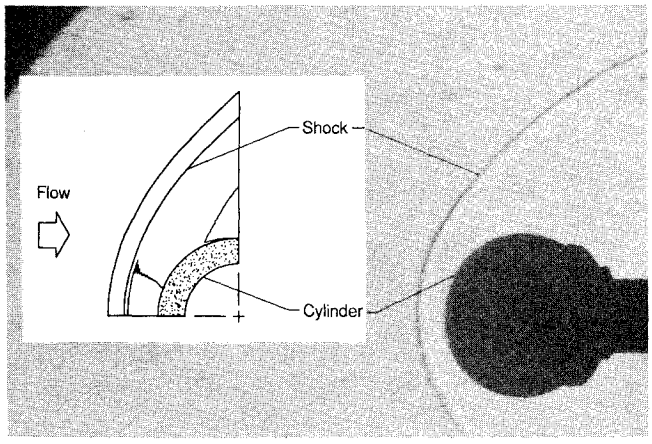

Fig. 4 Comparison of density contours with schlieren photograph for Mach 6.47 flow over a 3-in.-diam cylinder.

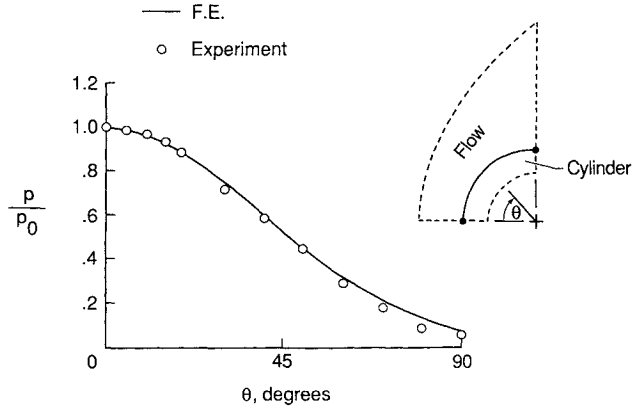

Fig. 5 Comparative surface pressure distributions on a 3-in.-diam cylinder subjected to Mach 6.47 flow.

configurations, the tunnel flow conditions, and the experimental results are given in Ref. 5.

The finite-element model representing the flow domain and the cylinder is shown in Fig. 3. Because of symmetry, only one-half of the incoming flow domain and one-fourth of the cylinder are modeled. The flowfield is characterized by the bow shock that stands off the cylinder and the thin boundary layer at the cylinder surface. Sharp gradients in the flow variables occur in these regions, hence closely spaced elements are required for resolution. In the remaining area between the body and bow shock, flow gradients are significantly smaller, hence element spacing can be larger. Since the flow structure is known a priori, the flowfield mesh is constructed to space elements closely together in the shock region and boundary layer. The elements are also densely packed along the stagnation line ($y = 0$). In this region close to the cylinder surface, the flow velocities are very small and become zero at the stagnation point. Away from the flow symmetry line, the subsonic flow accelerates nonuniformly to sonic speeds.

The finite-element model consists of 12,000 quadrilateral elements in the flow domain and 3000 quadrilateral elements for the cylinder with the same discretization along the flow-cylinder interface. A graded radial spacing was used in the cylinder. About 35% of the fluid elements lie in the 0.02-in.-thick boundary layer. The boundary-layer mesh is graduated normal to the cylinder surface by an incremental factor of 1.1. The smallest element is at the flow stagnation point and is only 0.0004-in. long in the direction normal to the cylinder surface. This extremely small element dimension is necessary to capture the temperature gradient and hence the aerodynamic heating rate.

Typical flow solutions are shown in Figs. 4–7. Predicted density contours are compared in Fig. 4 with an experimental

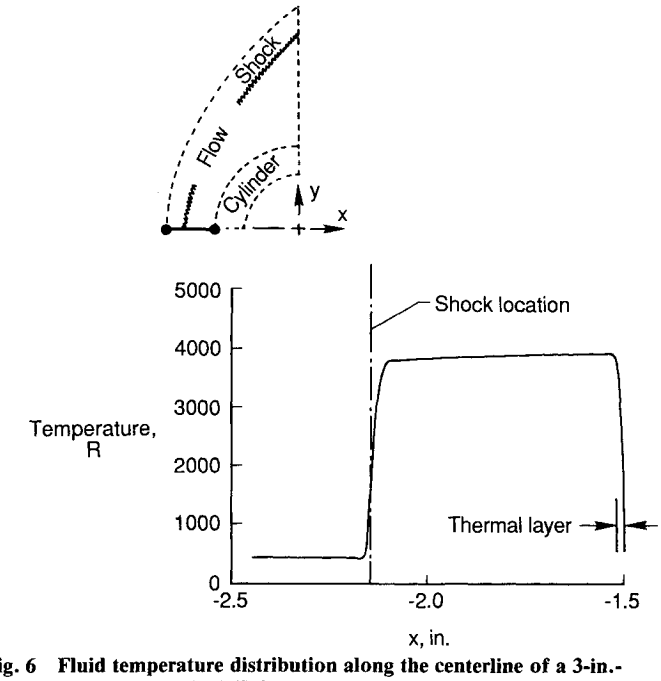

Fig. 6 Fluid temperature distribution along the centerline of a 3-in.-diam cylinder for Mach 6.47 flow.

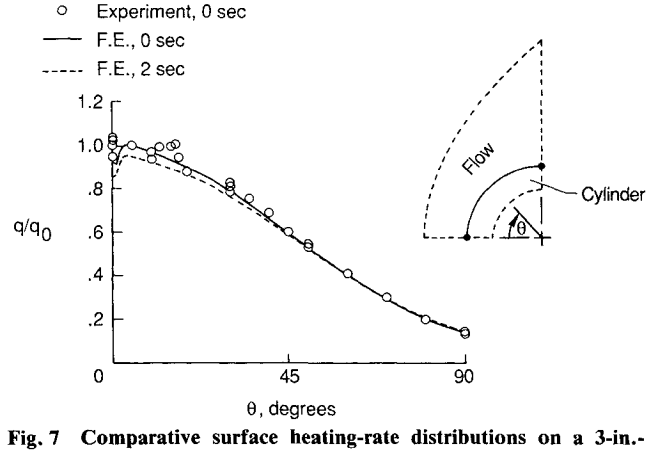

Fig. 7 Comparative surface heating-rate distributions on a 3-in.-diam cylinder subjected to Mach 6.47 flow.

schlieren photograph[5] that is also a measure of flow density. The comparison of the shock shape and position indicates that the global flowfield is reasonably well predicted. Figure 5 shows the excellent agreement between the computed aerodynamic pressure distribution along the cylinder surface and the experimental data.[6] The predicted and experimental pressures are normalized by their respective stagnation-point pressures, which were within 5% of each other.

The major difficulty in the fluid analysis is the prediction of the aerodynamic heating rates because a very accurate resolution of the flow temperature gradient normal to the cylinder surface is required. The computed flow temperature distribution (Fig. 6) along the flow symmetry line ($y = 0$) clearly illustrates the sharp gradients that must be resolved. The freestream temperature increases sharply from 435°R to about 3900°R across the bow shock. Within a very thin layer at the flow stagnation point, the temperature drops sharply from 3900°R to the surface temperature of 530°R. This steep temperature gradient within the thin layer, which is about 3% of the shock-layer thickness, produces a high stagnation-point heating rate. The predicted bow shock location compares well with the location predicted by empirical formulae[12] and the schlieren photograph (Fig. 4). The predicted heating-rate distribution normalized to the stagnation point heating rate at

time zero compares well with the experimental results[5] as shown in Fig. 7. The predicted stagnation point heating rate (42.5 Btu/ft^2-s) is in excellent agreement with the Fay and Riddell solution[13] (42.5 Btu/ft^2-s) and a viscous shock-layer solution[14] (41.4 Btu/ft^2-s), but is quite lower than the experiment[5] (61.7 Btu/ft^2-s). The difference between the predicted and the experimental heating rate is attributed to freestream turbulence in the test stream, which is not taken into account by the analysis.

Since the flowfield reaches equilibrium instantaneously compared to the thermal response of the cylinder, this aerodynamic analysis was updated at 2-s intervals. The cylinder temperature contours at 2 s are shown in Fig. 8. The figure shows that the maximum temperature of about 700°R occurs at the stagnation point, whereas the temperature along the back side of the cylinder remains at the ambient temperature of 530°R. The structure responds instantly to the pressure and temperature field, hence a quasistatic structural analysis is adequate to predict the cylinder deformations and thermal stresses. The structural boundary conditions and the resulting circumferential thermal-stress distribution on the cylinder are shown in Fig. 9. A maximum compressive stress of 32 ksi occurs on the cylinder outer surface near the stagnation point due to the high-temperature gradients in that region. The cylinder deformation is negligible compared to the cylinder diameter due to the relatively low-temperature change and hence has a negligible effect on the aerodynamic flow. However, the change in the surface temperature has a moderate effect at $t = 2$ s on the flowfield. The aerodynamic heating rate is reduced in the region where the surface temperature has increased as shown in Fig. 7, due to a thickening of the thermal boundary layer and a lower fluid temperature gradient at the cylinder surface. The stagnation-point heating rate decreased nearly 8% from the initial level with the cylinder temperature at 530°R.

A major difficulty encountered in the flowfield solution was the convergence of the aerodynamic heating rate. The aerodynamic heating rate, especially in the flow stagnation zone, converged slowly, because the small mesh needed to capture the high-temperature gradient required a very small time step to satisfy the computational stability criterion. Hence, coupled with low-flow velocities, perturbations take a large number of time steps to convect out of the flow domain. The coupling in this problem is moderate to weak and occurs primarily between the flow and thermal analyses. Since the flow and stress fields are not coupled and develop instantaneously compared to the structural temperature field, an iterative solution between disciplinary solutions would be adequate. Of course, the integrated analysis significantly eased data transfer between disciplinary analyses.

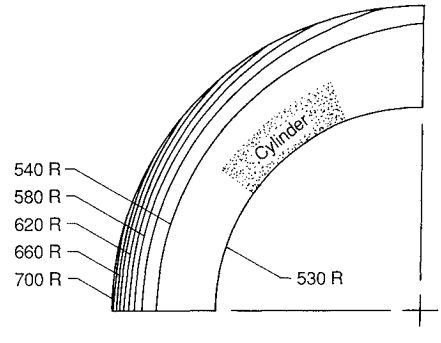

Fig. 8 Temperature contours on a 3-in.-diam cylinder at 2 s.

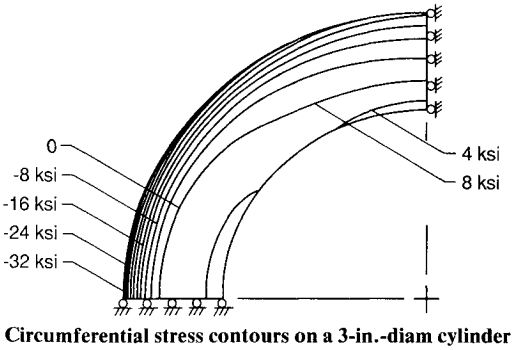

Fig. 9 Circumferential stress contours on a 3-in.-diam cylinder at 2 s.

Convectively Cooled Leading Edge

A 0.25-in.-diam leading edge is used in the second example to study and identify the issues related to the thermal-structural analysis and the design of convectively cooled leading edges subjected to intense aerodynamic heating. The example represents the acceleration of a hypersonic vehicle through Mach 16, which causes the vehicle nose bow shock to sweep across the engine cowl leading edge from an outboard to an inboard position. The sequence of events is classified into the three conditions shown in Fig. 10. For condition I, the oblique shock, representing the vehicle nose bow shock and created by the Mach 16 freestream flow, passes outboard of the cowl leading edge. At this condition, the cowl leading edge is exposed to the Mach 8 flow behind the Mach 16 shock wave. It should be noted that the aerodynamic heating rate on the leading edge at this Mach 8 flow (condition I) is higher than that at the Mach 16 flow (condition III) due to the additional compression of the flow as it passes through the oblique shock wave. As the vehicle continues to accelerate through Mach 16, the vehicle oblique shock wave moves across the cowl leading edge (condition II) intersecting with the leading-edge bow shock to produce transient shock wave interference heating. This interference heating results in a significant amplification of the heating rate on the leading edge as shown at typical times in Fig. 11. The envelope for the peak values and the distributions are idealizations of the experimental distribu-

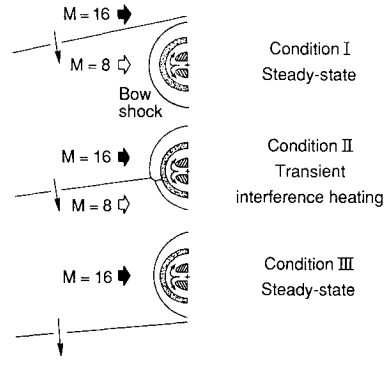

Fig. 10 A 0.25-in.-diam hydrogen-cooled leading edge with shock wave interference heating.

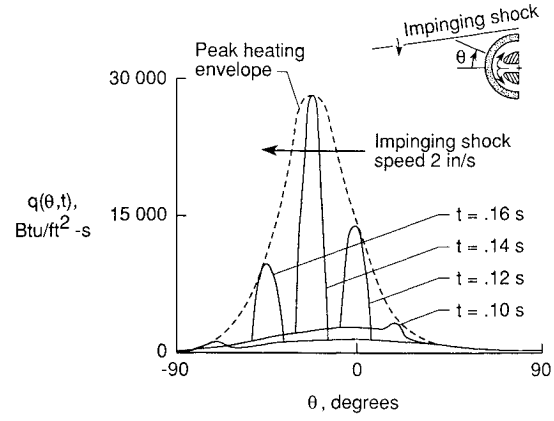

Fig. 11 Leading-edge transient interference heating due to vehicle acceleration at Mach 16.

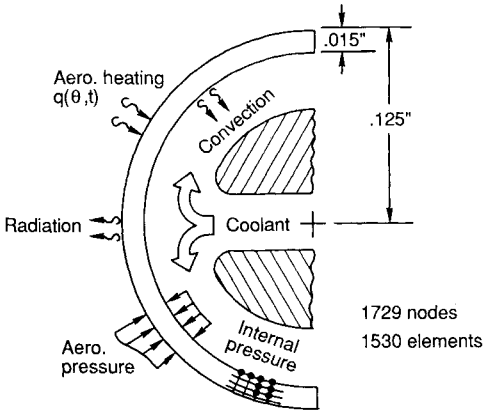

Fig. 12 A schematic thermal-structural finite-element model of 0.25-in.-diam leading edge with boundary conditions.

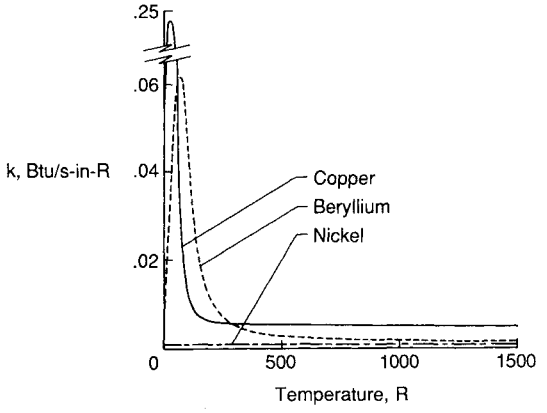

Fig. 13 Temperature-dependent thermal conductivity for copper, beryllium, and nickel.

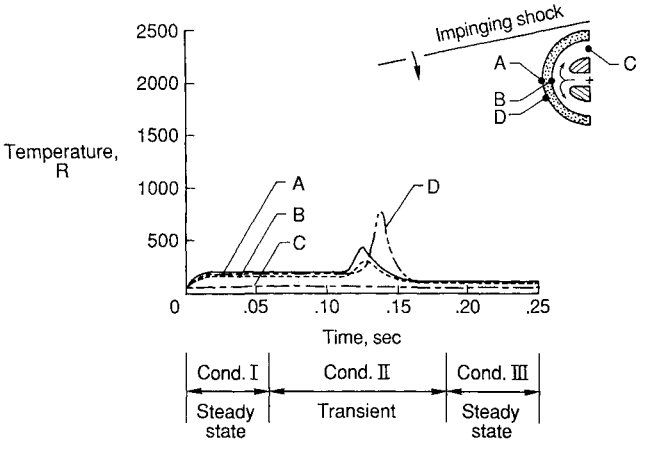

Fig. 14 Copper leading-edge temperature response.

tions given in Ref. 15. This idealization was used because the Taylor-Galerkin explicit-flow algorithm would have been prohibitively expensive to perform the analyses. The interference heating rate reaches a peak value about 22 deg below the horizontal centerline of the leading edge. The oblique shock is assumed to move at a speed of 2 in./s and passes the leading edge in 0.125 s. After the oblique shock passes, the leading edge is heated by the Mach 16 flow (condition III).

The leading-edge geometry, boundary conditions, and a schematic of the finite-element thermal-structural model are shown in Fig. 12. The leading-edge outer surface is subjected to the transient aerodynamic heating given in Fig. 11 and emits radiant energy to space. The inner surface is convectively cooled by the direct impingement of a sonic hydrogen jet stream with an inlet temperature of 50°R. The hydrogen flow rate is 0.104 lb_m/s and the coolant film coefficient is 8 Btu/ft^2-°R-s. The finite-element model consists of 1440 quadrilateral elements for the leading edge and 90 mass-transport conduction/surface convection elements representing the hydrogen coolant flow. The leading-edge mesh is graded in the radial direction similar to the cylinder mesh shown in Fig. 3 but is uniform in the circumferential direction.

Materials with "super" thermal conductivity are used to reduce the leading-edge temperature, the temperature gradients through the thickness, and increase circumferential diffusion of the heat load. Copper and beryllium are the candidate materials because they provide higher thermal conductivity than customary materials, such as nickel, as shown in Fig. 13. The thermal conductivity of these two materials are reported to be exceptionally high at low temperature.[16] The peaks of the thermal conductivity for copper and beryllium, which occur at 20°R and 70°R, are approximately 300 and 80 times higher than nickel, respectively. However the increased conductivity occurs over a very small temperature range, offering a significant challenge to the computational procedure.

The copper leading edge had better thermal-structural performance[17] and is presented herein. The initial leading-edge temperature was assumed to be equal to the coolant temperature of 50°R. Figure 14 shows the leading edge and coolant temperature histories at the selected locations shown in the inset during the sequence of events. At the early time, the leading edge is first subjected to the Mach 8 flow (condition I) for $0 \text{ s} < t < 0.06$ s. The figure shows that the steady-state condition is reached at the end of this time interval, and the maximum temperature of about 200°R occurs at the horizontal centerline on the outer surface of the leading edge (location A). The inner surface (location B) is at a lower temperature of 150°R due to heat convection to the hydrogen coolant. As the hydrogen coolant flows along the coolant passage, its temperature increases from the inlet temperature of 50°R to 73°R at the exit (location C).

During the transient interference heating (condition II, $0.06 \text{ s} < t < 0.185$ s), the outer surface temperature at the centerline (location A) peaks at 395°R at the time of the oblique shock impingement ($t = 0.12$ s). The maximum surface temperature of approximately 766°R occurs at 22 deg below the centerline (location D) due to the maximum localized heating at $t = 0.14$ s. As the oblique shock passes ($t > 0.185$ s), the leading edge is heated by the Mach 16 flow (condition III). The leading-edge temperature drops due to the lower aerodynamic heating at this condition. Details of the leading-edge temperature distributions as the shock sweeps across the leading edge are shown at the selected times in Figs. 15a-d.

The most severe thermal load on the copper leading edge, which occurs at the time of the peak aerodynamic heating ($t = 0.14$ s in Fig. 15c), is used in the structural analysis to study the leading-edge response. Since the thermal and structural models were identical, the transfer of nodal temperatures to the structural analysis was straightforward. Temperature-dependent material strength properties for copper are included in the analysis. A hydrogen coolant pressure of 1000 psi is assumed to apply uniformly along the leading-edge inner surface. Along the outer surface, the aerodynamic pressure distribution is assumed to be the same shape as the aerodynamic heating[15] with a peak pressure of 1000 psi. These pressure distributions and the structural boundary conditions are superimposed on the predicted leading-edge structural response shown in Fig. 16. The figure shows the circumferential stress distribution on the deformed leading edge. The deformed leading edge shown in this figure is greatly exaggerated to highlight the detail of the deformed shape. At the oblique shock impingement location where the peak temperature and temperature gradients occur, the radial deformation is 0.0005 in., and the maximum compressive stress is 25 ksi. In other regions of the leading edge, the circumferential stress is moderate, varying from 10 ksi in tension to 10 ksi in compression.

The structural analysis was performed in two dimensions assuming plane strain. Although this is a conservative assump-

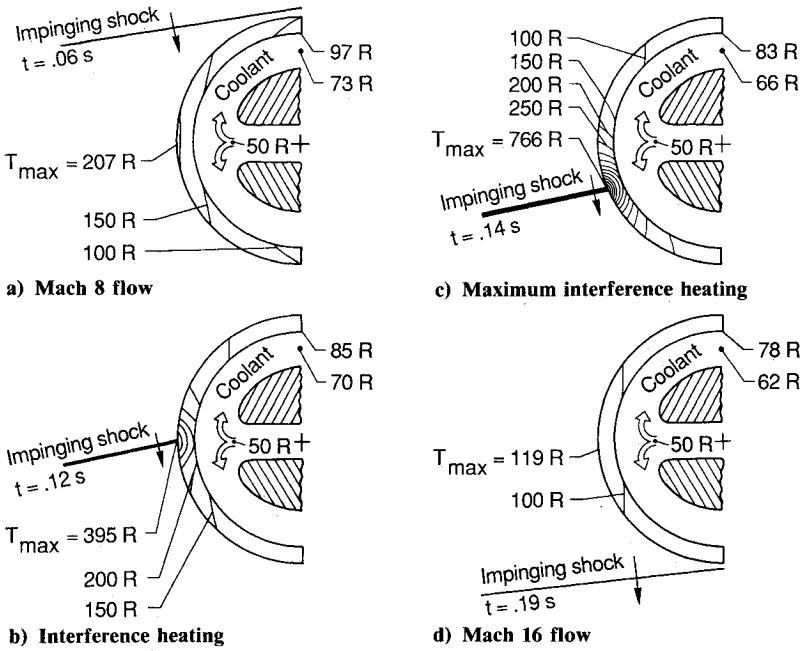

Fig. 15 Temperature contours for copper leading edge.

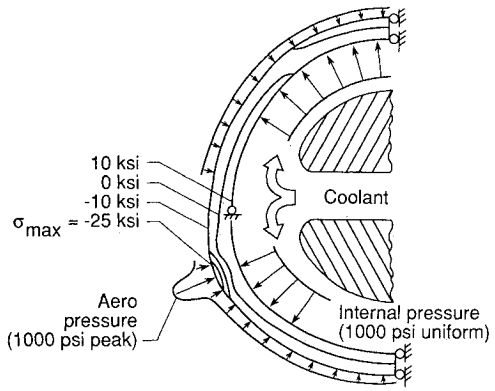

Fig. 16 Loads and circumferential stress contours on deformed copper leading edge at maximum interference heating.

tion, it clearly indicates the extreme axial compressive stresses (~ 100 ksi) that occur in the leading edge due to the extreme circumferential temperature gradient. The analysis suggests that the axial stresses for a three-dimensional model of the leading edge may exceed the elastic limit of the material. The structural response shows that the peak circumferential stress occurs at the oblique shock impingement location where the temperature and its gradients are maximum. The very high temperature and stresses could result in the failure of the leading edge, hence a more sophisticated structural analysis may be needed to include the capability to predict the permanent localized deformation, including time-dependency effect such as cyclic loading and creep, as the oblique shock moves across the leading edge.

Concluding Remarks

Applications of a finite-element approach for integrated fluid-thermal-structural analysis of aerodynamically heated leading edges were presented. The Navier-Stokes equations for high-speed compressible flow and the associated thermal-structural equations were solved using a single finite-element approach in one integrated, vectorized computer program. The approach was used to study and validate the prediction of the flow behavior and the aerothermal loads by comparing with experimental data for Mach 6.47 flow over a 3-in.-diam stainless steel cylinder. Comparison with experimental pressure and heat-flux distributions is excellent. The thermal and structural analyses for the cylinder were performed, and the response was examined to investigate benefits of the integrated interdisciplinary analysis and coupling. The coupling caused by the cylinder deformation that could alter the flowfield was negligible. The fluid-thermal coupling from the increase in the cylinder temperature, which results in a reduction of the aerodynamic heating, was moderate but significant. The aerodynamic heating using the explicit Taylor-Galerkin algorithm converged very slowly because of the small time steps required for computational stability. A more efficient fluid analysis procedure is needed to speed up the convergence rate in the aerodynamic heating computation.

Critical issues for the thermal-structural analysis were demonstrated by the analyses of a hydrogen-cooled leading edge subjected to intense aerodynamic heating. The use of superthermal conductivity materials alleviates the elevated leading-edge temperatures and gradients and hence the stress levels. The approach clearly demonstrates the ability to perform transient nonlinear thermal analysis for problems with highly nonlinear temperature-dependent material properties and various boundary conditions. Under severe aerothermal loads, which can cause intense localized leading-edge temperatures, the present analysis indicates the need for a three-dimensional thermoviscoplastic analysis to accurately predict the time-dependent structural response.

The applications have demonstrated the fundamental capability of the integrated analysis approach to 1) provide insight into the features of the hypersonic flow over the leading edge, the leading-edge thermal-structural response and their interactions, 2) reduce manpower requirements, and 3) increase the computational efficiency for coupled interdisciplinary problems.

References

[1]Shideler, J. L., Webb, G. L., and Pittman, C. M., "Verification Tests of Durable Thermal Protection System Concepts," *Journal of Spacecraft and Rockets,* Vol. 22, Nov.-Dec. 1985, pp. 598-604.

[2]Olsen, G. C. and Smith, R. E., "Analysis of Aerothermal Loads on Spherical Dome Protuberances," *AIAA Journal,* Vol. 23, May 1985, pp. 650-656.

[3]Glass, C. E. and Hunt, L. R., "Aerothermal Tests of Spherical Dome Protuberance on a Flat Plate at a Mach Number of 6.5," NASA TP-2631, Dec. 1986.

[4]Thornton, E. A. and Dechaumphai, P., "Coupled Flow, Thermal and Structural Analysis of Aerodynamically Heated Panels," *Journal of Aircraft,* Vol. 25, Nov. 1988, pp. 1052–1059.

[5]Wieting, A. R., "Experimental Study of Shock Wave Interference Heating on a Cylindrical Leading Edge," NASA TM-100484, May 1987.

[6]White, F. M., *Viscous Fluid Flow,* McGraw-Hill, New York, 1974, pp. 28–29.

[7]Thornton, E. A. and Wieting, A. R., "Finite Element Methodology for Transient Conduction/Forced Convection Thermal Analysis," *Progress in Astronautics and Aeronautics: Heat Transfer, Thermal Control and Heat Pipes,* Vol. 70, edited by Walter B. Olstad, AIAA, New York, 1980, pp. 77–103.

[8]Christie, I., Griffiths, D. F., Mitchell, A. R., and Sanz-Serna, J. M., "Product Approximation for Non-linear Problems in the Finite Element Method," *IMA Journal of Numerical Analysis,* Vol. 1, July 1981, pp. 253–266.

[9]Bey, K. S., Thornton, E. A., Dechaumphai, P., and Ramakrishnan, R., "A New Finite Element Approach for Prediction of Aerothermal Loads—Progress in Inviscid Flow Computations," NASA TM-86434, July 1985.

[10]Thornton, E. A. and Dechaumphai, P., "A Taylor-Galerkin Finite-Element Algorithm for Transient Nonlinear Thermal-Structural Analysis," AIAA Paper 86-0911, May 1986.

[11]Thornton, E. A., Dechaumphai, P., and Vermaganti, G., "A Finite-Element Approach for Prediction of Aerothermal Loads," AIAA Paper 86-1050, May 1986.

[12]Billig, F. S., "Shock-Wave Shapes Around Spherical and Cylindrical-Nosed Bodies," *Journal of Spacecraft and Rockets,* Vol. 4, June 1967, pp. 822–823.

[13]Fay, J. A. and Riddell, F. R., "Theory of Stagnation Point Heat Transfer in Dissociated Air," *Journal of the Aeronautic Sciences,* Vol. 25, Feb. 1958, pp. 73–85.

[14]Holcomb, J. E., Curtis, J. T., and Shope, F. L., "A New Version of the CVEQ Hemisphere Viscous Shock Layer Program for Equilibrium Air," Arnold Engineering Development Center, Arnold Air Force Station, TN, AEDC-TMR-85-V7, Feb. 1985.

[15]Holden, M. S., Wieting, A. R., Moselle, J. R., and Glass, C., "Studies of Aerothermal Loads Generated in Regions of Shock/Shock Interaction in Hypersonic Flow," AIAA Paper 88-0477, Jan. 1988.

[16]Touloukian, Y. S., Powell, R. W., Ho, C. Y., and Klemens, P. G., "Thermal Conductivity for Metallic Elements and Alloys," *Thermophysical Properties of Matter,* Vol. 1, IFI/Plenum, New York, 1970, pp. 68–81.

[17]Dechaumphai, P., Thornton, E. A., and Wieting, A. R., "Flow-Thermal-Structural Study of Aerodynamically Heated Leading Edges," AIAA Paper 88-2245, April 1988.

June 26, 1989

Candidates Solicited for *JSR* Editor-in-Chief Post

On January 1, 1990, AIAA will appoint a new Editor-in-Chief of its *Journal of Spacecraft and Rockets (JSR)*, and solicits candidates for this prestigious editorial post.

The selection committee to replace Dr. Frank J. Redd, who will be retiring from the position of Editor in Chief as of December 31, 1989, will be chaired by Earl. H. Dowell, a past Vice President – Publications. Other members of the selection committee include Allen E. Fuhs, William H. Heiser, and Paul F. Holloway. Fuhs and Heiser have also served terms as VP – Publications.

To apply for the editorship, submit four copies of an application citing qualifications and your objectives for the journal to:

Prof. Earl H. Dowell
c/o Norma Brennan
AIAA Headquarters
370 L'Enfant Promenade, S.W.
Washington, D.C. 20024-2518

*The deadline for applications will be **September 30, 1989.***

JSR now has the following scope:

"This journal is devoted to reporting advancements in the science and technology associated with spacecraft and tactical and strategic missile systems, including subsystems, applications, missions, environmental interactions, and space sciences. The Journal publishes original archival papers disclosing significant developments in spacecraft and missile configurations, system and subsystem design and application, mission design and analysis, missile and spacecraft aerothermodynamics, space instrumentation, developments in space sciences, space processing, and manufacturing, space operations, and applications of space technologies to other fields. The context of the Journal also includes ground-support systems, manufacturing, integration and testing, launch control, recovery, and repair, space communications, and scientific data processing. Papers also are sought which describe the effects on spacecraft and missile design and performance of propulsion, guidance and control, thermal management, and structural systems."

Duties of the Editor-in-Chief encompass the following: Foreseeing and stimulating major contributions to the journal, with assistance from an Editorial Advisory Board. Logging in, acknowledging, and appraising submitted manuscripts; checking their general quality, importance to the technical community, and compliance with editorial specifications; assigning them to Associate Editors for processing; arbitrating editorial disputes; tracking manuscripts and Associate Editor actions via computer.

The post carries an honorarium of $225 per month and reimbursement for allowable expenses up to a maximum of $3,400 per year.

Address questions about editing procedures or other factors connected with duties to: Norma Brennan, AIAA Director, Editorial and Production Departments (202-646-7482).

Questions concerning policy may be directed to me in writing at the following address: Dr. Billy M. McCormac, AIAA Vice President – Publications, D91-01/B256, Lockheed R&DD, 3251 Hanover Street, Palo Alto, CA 94304 **B. M. M.**